Solar-driven upgrading of 5-hydroxymethylfurfural on BiVO$_4$ photoanodes: Effect of TEMPO mediator and cocatalyst on reaction kinetics

Lingxia Zheng [a,b,*], Penghui Xu [a], Yujuan Zhao [a], Zhenyu Bao [a], Xingyu Luo [a], Xiaowei Shi [a,b], Qi Wu [c,**], Huajun Zheng [a,b,*]

[a] *Department of Applied Chemistry, Zhejiang University of Technology, Hangzhou 310014, PR China*
[b] *Petroleum and Chemical Industry Key Laboratory of Organic Electrochemical Synthesis, State Key Laboratory Breeding Base of Green Chemistry Synthesis Technology, Zhejiang University of Technology, Hangzhou 310014, PR China*
[c] *School of Science and Institute of Oxygen Supply and Everest Research Institute, Tibet University, Lhasa 850000, PR China*

ARTICLE INFO

ABSTRACT

Biomass upgrading driven by solar energy in a photoelectrochemical (PEC) cell offers an energy-saving and cost-effective alternative route to yield value-added products. Herein, we report remarkably efficient solar-driven TEMPO mediated 5-hydroxymethylfurfural (HMF) oxidation over NiFe-LDH/BiVO$_4$ photoanodes: yield of 2,5-furandicarboxylic acid (FDCA) and faradaic efficiency increase from 1.7 %/2.5 % over BiVO$_4$ to ~100 %/100 % over 1-LDH/BiVO$_4$ at 0.7 V$_{RHE}$, demonstrating boosted catalytic efficiency and utility of PEC cells. The distinctly larger surface potential difference (1.5 times) validates the effective charge separation and transfer in 1-LDH/BiVO$_4$, and more holes can be available to oxidize TEMPO. The effect of TEMPO is carefully investigated and it suggests that TEMPO-mediated PEC oxidation of HMF is thermodynamically and kinetically favorable in contrast to water oxidation. Superb reactivity can be achieved with an increase of TEMPO concentration. This work demonstrates that solar-driven biomass upgrading can be a feasible anode reaction for solar-fuel production by replacing the sluggish water oxidation process.

1. Introduction

Solar-driven photoelectrochemical (PEC) water splitting into hydrogen and oxygen is one of the most popular strategies to convert solar energy toward sustainable energy [1–5]. The water oxidation half reaction at the anode is considered to be the rate-determining step in the overall water splitting due to kinetically sluggish multistep proton-coupled electron transfer process. Large overpotentials are required and scarce expensive noble metal-based catalysts are employed, which hinders the large-scale application in industry. In addition, the produced oxygen is not of significant value. Therefore, the development of kinetically and thermodynamically favorable anode reaction to yield value-added products is beneficial to the utility and efficiency of PEC cells [6–8].

An exciting and promising strategy is to pair hydrogen evolution reaction (HER) with anodic oxidation of biomass-derived intermediates (e.g., alcohols and aldehydes) [9–17]. In particular, 5-hydroxymethyl-furfural (HMF), a key platform molecule derived from C6

monosaccharides that can yield a large variety of industrially important value-added chemicals via further conversion. One of its oxidation products, 2,5-furandicarboxylic acid (FDCA) is considered to be a possible replacement for terephthalic acid, a much valuable precursor for biobased polymers [18–20]. In light of this, huge attention has been paid to the oxidation of HMF into FDCA. For instance, Choi K.-S. et al. demonstrated the PEC conversion of HMF to FDCA over BiVO$_4$ photo-anode using TEMPO (2,2,6,6-tetramethylpiperidine-1-oxyl) as a redox mediator [21]. They obtained remarkable reaction selectivity and ~100 % faradaic efficiency (FE) but requiring a considerable external potential (1.04 V$_{RHE}$). Chadderdon D. J. at al.[22] reported that 88 % yield of FDCA was achieved over BiVO$_4$/CoPi (cobalt phosphate) bilayer photo-anode, demonstrating the viability of using heterostructure photo-anodes for solar-driven biomass conversion. Kawde A. et. al.[23] investigated the pH effect on the reaction selectivity over modified Fe$_2$O$_3$ photoanode and found that 90.7 % yield of FDCA was achieved at 1.1 V$_{RHE}$ in alkaline media (pH=12.5). Inspired by these accomplishments, the rational design of heterostructure photoanodes for efficient

---

biomass upgrading through PEC cells is highly encouraged and the role of TEMPO mediator also needs more exploration.

As one of most promising semiconductor oxide with an appropriate valance band position for water oxidation, $BiVO_4$ is extensively investigated as a photoanode in PEC cells [24–26]. It has been well established that surface modification of $BiVO_4$ such as CoPi [27], BP quantum dots, transition metal oxyhydroxides, and Co_3O_4 [28], turns out to be an effective strategy to alleviate the charge recombination loss [29–31], and thereby promoting water oxidation. However, such modification might not be applicable for improving redox mediated alcohol oxidation as it was presumed that it would favor water oxidation over mediator oxidation[32]. Herein, we demonstrate that nanoporous $BiVO_4$ films modified with NiFe-LDH, a distinguished OER (oxygen evolution reaction) electrocatalyst [33–35], can effectively boost the TEMPO-mediated HMF photooxidation over water oxidation and TEMPO oxidation. A remarkable cathodic onset potential shift (370 mV) and significantly enhanced photocurrent (6 times higher) at 0.7 V_{RHE} are achieved on 1-LDH/$BiVO_4$ compared with those of pristine $BiVO_4$. Kelvin probe force microscopy (KPFM) and photoluminescence spectra (PL) are employed to visualize the spatial distribution and interfacial transfer of photogenerated carriers. The effective charge separation enables a significantly increase of FDCA yield (from 1.7 % to ~100 %) and FE (from 2.5 % to ~100 %), exhibiting boosted efficiency and utility of PEC cells for solar-driven biomass upgrading. Moreover, superb reactivity with boosted FE can be achieved with an increase of TEMPO concentration. ~100 % yield of FDCA with ~100 % FE can be achieved at a significantly reduced potential (0.6 V_{RHE}) in a higher TEMPO concentration (5 mg mL^{-1}), which suggests that the unbiased PEC oxidation

of HMF at anode and hydrogen production at the cathode might be achieved with an optimal concentration of redox mediator and rational design of photoelectrodes. This work demonstrates that TEMPO-mediated PEC oxidation might be applicable for other biologically derived substrates.

2. Experimental section

2.1. Preparation of BiVO₄

Bi(NO₃)₃·5 H₂O (0.9701 g, 0.04 M) was dissolved in KI solution (50 mL, 0.4 M) and the pH was adjusted by nitric acid to be 1.7. Then it was mixed with 20 mL *p*-benzoquinone (0.5126 g, 0.23 M) ethanol solution. The pristine BiVO₄ photoanode was prepared through a cathodic deposition process at − 0.1 V vs. Ag/AgCl (300 s) on FTO substrate to give BiOI film. Then, 0.1 mL of dimethyl sulfoxide containing 0.4 M vanadium oxide acetylacetonate solution was dropped onto the surface of BiOI film, and then it was heated in air at 450 °C for 2 h to produce BiVO₄. Afterwards, the sample was soaked in 1 M NaOH solution for 45 min to give BiVO₄ electrode with a loading amount of 8.3 mg.

2.2. Preparation of LDH/BiVO₄

Typically, Ni(NO₃)₂·6 H₂O (0.5 mmol) and Fe(NO₃)₃·9 H₂O (0.06 mmol) were dissolved under magnetic stirring in 80 mL of deionized water containing urea (2.5 mmol) and NH₄F (1.0 mmol). The mixture was poured to a Teflon-lined stainless-steel autoclave containing BiVO₄ electrode inside. It was heated at 120 °C for 6 h. After reaction, the
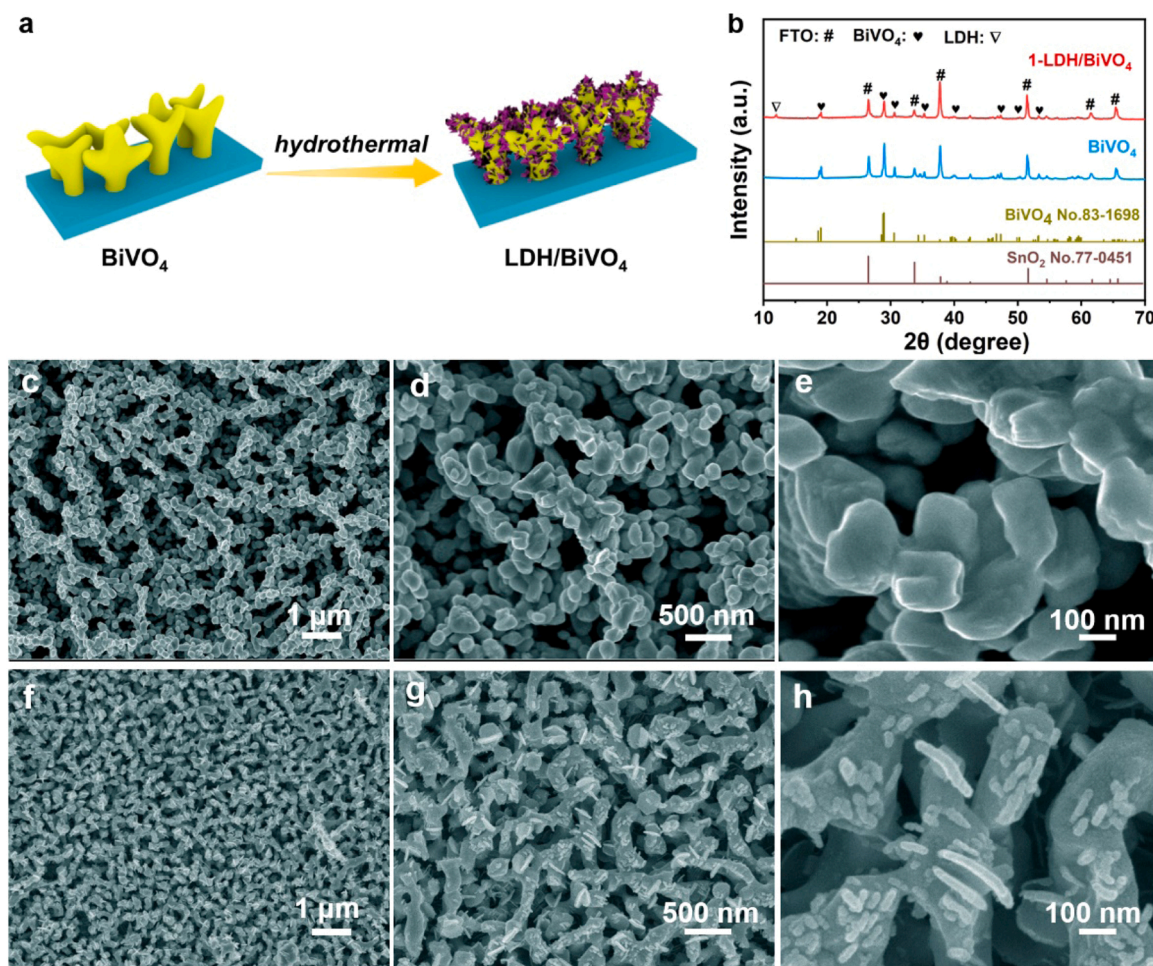

Fig. 1. (a) Schematic illustration for the synthesis of LDH/BiVO₄ electrode. (b) XRD patterns. SEM images of (c-e) BiVO₄ and (f-h) 1-LDH/BiVO₄.

sample was taken out and rinsed with ethanol, and the electrode was termed as 1-LDH@BiVO$_4$ after drying at 60 °C in the vacuum oven (Fig. 1a). To tailor the loading amounts of NiFe-LDH, Ni and Fe salts with different dosages were added (0.25 mmol Ni(NO$_3$)$_2$·6 H$_2$O and 0.03 mol Fe(NO$_3$)$_3$·9 H$_2$O, 1.0 mmol Ni(NO$_3$)$_2$·6 H$_2$O and 0.12 mmol Fe (NO$_3$)$_3$·9 H$_2$O, 2.0 mmol Ni(NO$_3$)$_2$·6 H$_2$O and 0.24 mmol Fe(NO$_3$)$_3$·9 H$_2$O), and the obtained samples were termed as 0.5-LDH/BiVO$_4$, 2-LDH/ BiVO$_4$ and 4-LDH/BiVO$_4$, respectively. The photographs of different composite electrodes were displayed in Fig. S1. The loading amount was measured to be 11.7, 15.0, 21.2, 22.4 mg for 0.5-LDH/BiVO$_4$, 1-LDH/ BiVO$_4$, 2-LDH/BiVO$_4$ and 4-LDH/BiVO$_4$, respectively.

2.3. Characterization

Scanning electron microscope (SEM, Zeiss SUPRA 55) and transmission electron microscope (TEM, Philips-FEI Tecnai G2F30 S-Twin) were performed to examine the structural morphology. X-ray diffraction patterns (XRD, PANalytical X′Pert PRO) and X-ray photoelectron spectroscopy (XPS, Thermo Scientific K-Alpha, USA) were performed to examine the crystalline structure and chemical states, respectively. UV–vis diffuse reflectance spectra (DRS, Shimadzu UV-2700 spectrometer) were performed to examine the optical properties. Photoluminescence (PL) spectroscopy was tested at an excitation wavelength of 310 nm on a Shimadzu RF-6000 fluorescence spectrophotometer. Kelvin probe force microscopy (KPFM, Bruker Dimension Icon) was used to examine the spatial charge distribution of electrodes in an amplitude-modulated mode. The tip (SCM-PIT-V2) was adopted with a spring constant of 3 N m^{-1} and resonant frequency of 75 kHz. The lift height was set to 100 nm and the AC voltage of 0.5 V. The light irradiated on the sample with a grazing angle of~5–10° was from a 470 W lamp (BBZM-III) with an output intensity of illumination $\geq$ 5800.0 LUX.

2.4. PEC measurements

PEC tests were conducted on a CHI 760D electrochemical workstation in a H-type cell with a Nafion 117 proton exchange membrane and a three-electrode configuration using BiVO$_4$ photoanode (back illumination), Ag/AgCl electrode and Pt as working, reference and counter electrode, respectively. The cathode chamber contained 0.5 M borate buffer solution with a pH of 9.0 (NaBi) while the anode chamber contained NaBi solution mixed with TEMPO and 5 mM HMF. All the potentials used in this study were referred to reversible hydrogen electrode (RHE) using the equation unless otherwise stated: $V_{RHE} = V_{Ag/AgCl} + 0.1976 V + 0.0592 \times pH$. A 300 W Xenon lamp was used to simulate the solar light with an AM 1.5 G filter (100 mW cm^{-2}). Linear sweep voltammograms (LSV) at 10 mV s^{-1} and transient response under chopped light were carried out. Mott-Schottky plots were tested under dark at 1000 Hz from 0 to 1.2 V$_{RHE}$.

2.5. Product analysis

The continue HMF oxidation was conducted at constant potential under light illumination in 0.5 M NaBi containing TEMPO and 5 mM HMF. The concentration of HMF and its oxidation products were analyzed by high performance liquid chromatography (HPLC, Agilent 1260 Infinity II) equipped with an AQ-C18 column and VWD detector, and they were quantified by external standard calibration curves (Fig. S2). The eluent was a mixture of 5 mM ammonium acetate and methanol (3:1 v/v) at a flow rate of 0.5 mL min^{-1}. The following equations were applied to calculate the conversion (Conv.) of HMF, selectivity (Sel.) of FDCA and yield of oxidation products and the Faradaic efficiency (FE):

$$\text{Conv.} = \frac{\text{moles of HMF reacted}}{\text{moles of initial HMF}} \times 100\% \tag{1}$$

$$\text{Sel.} = \frac{\text{moles of oxidation product}}{\text{moles of HMF reacted}} \times 100\% \tag{2}$$

$$\text{Yield} = \frac{\text{moles of oxidation product}}{\text{moles of initial HMF}} \times 100\% \tag{3}$$

$$\text{FE} = \frac{\text{mole of FDCA}}{\text{total passed charge}/(6 \times F)} \times 100\% \tag{4}$$

where F was the Faraday constant (96 485 C mol^{-1}).

2.6. Calculation method

Spin-polarized density functional theory (DFT) calculation was performed by adopting Vienna Ab-initio Simulation Package (VASP) package[36]. The electronic exchange and correlation effects were described within generalized gradient approximation (GGA) with the Perdew-Burke-Ernzerhof (PBE) functional [37–39] way. The DFT-D3 method of the Grimme's scheme was used to correct the Van Der Waals interactions between electrode and HMF/TEMPO molecules[40]. The HMF/TEMPO adsorbate structures were relaxed in a $20 \times 20 \times 20$ Å^3 box fully. In addition, Brillouin zones were $2 \times 2 \times 1$ Monkhorst-Pack meshes for the geometry optimization of BiVO$_4$ (010) surface and LDH/BiVO$_4$ heterostructure. The cutoff energy of the plane wave basis, energy and residual force convergence tolerances were set as 500 eV, 10^{-5} eV and 0.02 eV Å^{-1}, respectively. A vacuum distance of 15 Å was used to avoid interactions between two periodic units.

3. Results and discussion

3.1. Study of microstructures

Fig. 1a illustrates the preparation process of LDH/BiVO$_4$ photoanode through a facile hydrothermal method. The loading amounts and microstructures of NiFe-LDH are controlled by varying the contents of Ni and Fe salt precursors. The photographs of different LDH/BiVO$_4$ photoanodes are displayed in Fig. S1, which shows that the color of electrode changes from bright yellow to orange upon increasing the loading of NiFe-LDH. The crystallographic structures verified by XRD are presented in Fig. 1b and Fig. S3, which reveals pure monoclinic BiVO$_4$ phase (JCPDS No. 83-1698). The new diffraction peak at 11.53° matches well with the (003) plane of NiFe-LDH (JCPDS No.51-0463) in 1-LDH/ BiVO$_4$, suggesting the successful loading of NiFe-LDH [41]. The structure of nanoporous BiVO$_4$ (Fig. 1c-e) is consistent with the morphology of nanoporous BiVO$_4$ reported in literature [42], which consists of many particles with size ranging from 150 to 300 nm connected with each other with very clean surface. They are packed evenly with a large density on the surface of FTO. For 1-LDH/BiVO$_4$ (Fig. 1f-h), many stripe-like nanostructures are coated on the surface of BiVO$_4$, and the mapping results confirm the existence of V, O, Bi, Ni, and Fe entities (Fig. S4). Upon changing the metal salt precursors, three different LDH/BiVO$_4$ electrodes were prepared and the SEM images (Fig. S5) indicate that sporadic flower-like NiFe-LDH made of nanoflakes can be observed at a lower concentration of Ni-Fe salts for 0.5-LDH/BiVO$_4$ (Fig. S5a-c), while this morphology tends to fracture and forms nano-stripes/flakes for 2-LDH/BiVO$_4$ (Fig. S5d-f) and finally nanoparticulate film with a large density for 4-LDH/BiVO$_4$ (Fig. S5g-i) at a much higher concentration of Ni-Fe salts. i.e., The morphology of NiFe-LDH becomes small and distributes evenly with a large density over the surface of BiVO$_4$ when the concentration of NiFe salts increases gradually.

TEM image further reveals the porous nature of BiVO$_4$ and the LDH layer is anchored on BiVO$_4$ particles (Fig. 2a,b), consistent with SEM results. The distinct lattice fringes with spacing of 0.251 nm and 0.241 nm are respectively assigned to (020) plane of BiVO$_4$ and (101) plane of NiFe-LDH (Fig. 2c,d), agreeing well with XRD results. The EDS-
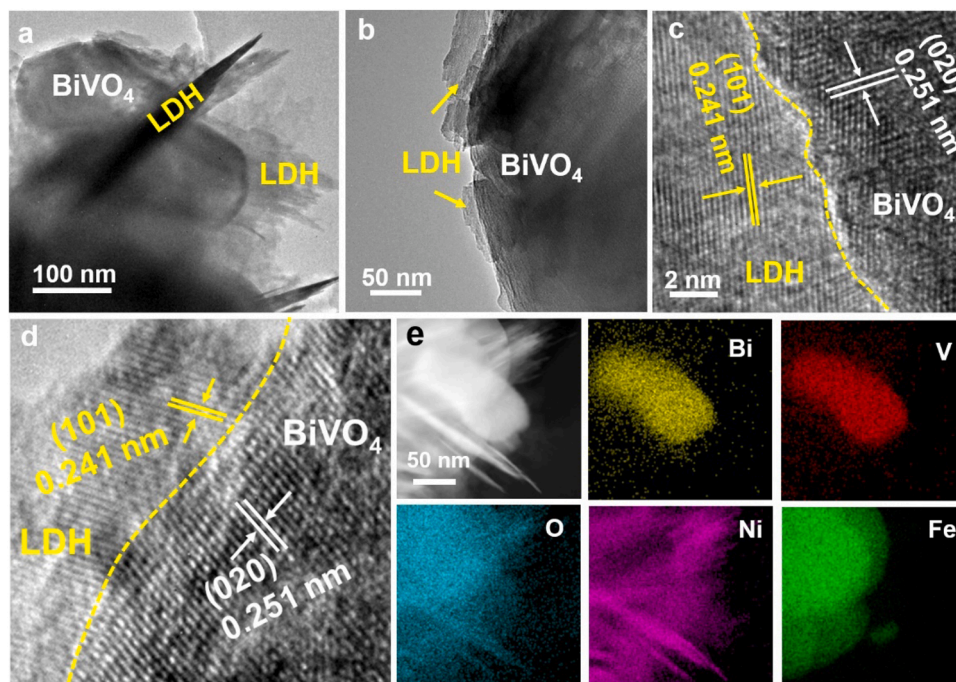
Fig. 2. (a,b) TEM images, (c,d) HR-TEM images and (e) mapping of 1-LDH/BiVO$_4$.

mapping (Fig. 2e) detects evident signals of Bi, V, O, Ni, and Fe, further suggesting the homogeneous distribution of NiFe-LDH on BiVO$_4$ crystals.

The survey spectrum of 1-LDH/BiVO$_4$ confirms the existence of Ni, Fe, V, Bi and O elements (Fig. 3a), implying the successful loading of LDH, in line with the EDS-mapping. The binding energies at 873.3 and 855.7 eV with a spin-energy difference of 17.6 eV are attributed to Ni $2p_{1/2}$ and Ni $2p_{3/2}$ orbitals (Fig. 3b), imply the Ni^{2+} oxidation states in NiFe-LDH [43], which is accompanied by two shake-up satellites (termed "*Sat.*") at 861.5 and 879.7 eV. Two characteristic peaks at

724.7 and 711.7 eV are belonged to Fe $2p_{1/2}$ and Fe $2p_{3/2}$ spin orbitals (Fig. 3c), respectively, manifesting the presence of Fe^{3+} oxidation states in NiFe-LDH [6,35,44]. The O 1 s spectra (Fig. 3d) can be deconvoluted into three peaks with binding energies at 529.2 eV, 531.1 eV and 533.2 eV, which are attributed to metal-O bond (O1), oxygen coordination (unsaturated oxygen, O2) and OH species of surface-adsorbed water (O3), respectively in BiVO$_4$. The much stronger peak at 531.1 eV in 1-LDH/BiVO$_4$ compared to that in BiVO$_4$ counterpart faithfully confirms the more oxygen defects in hybrid photoanode. Binding energies at 158.6 and 163.9 eV (Fig. 3e) are belonged to Bi^{3+}
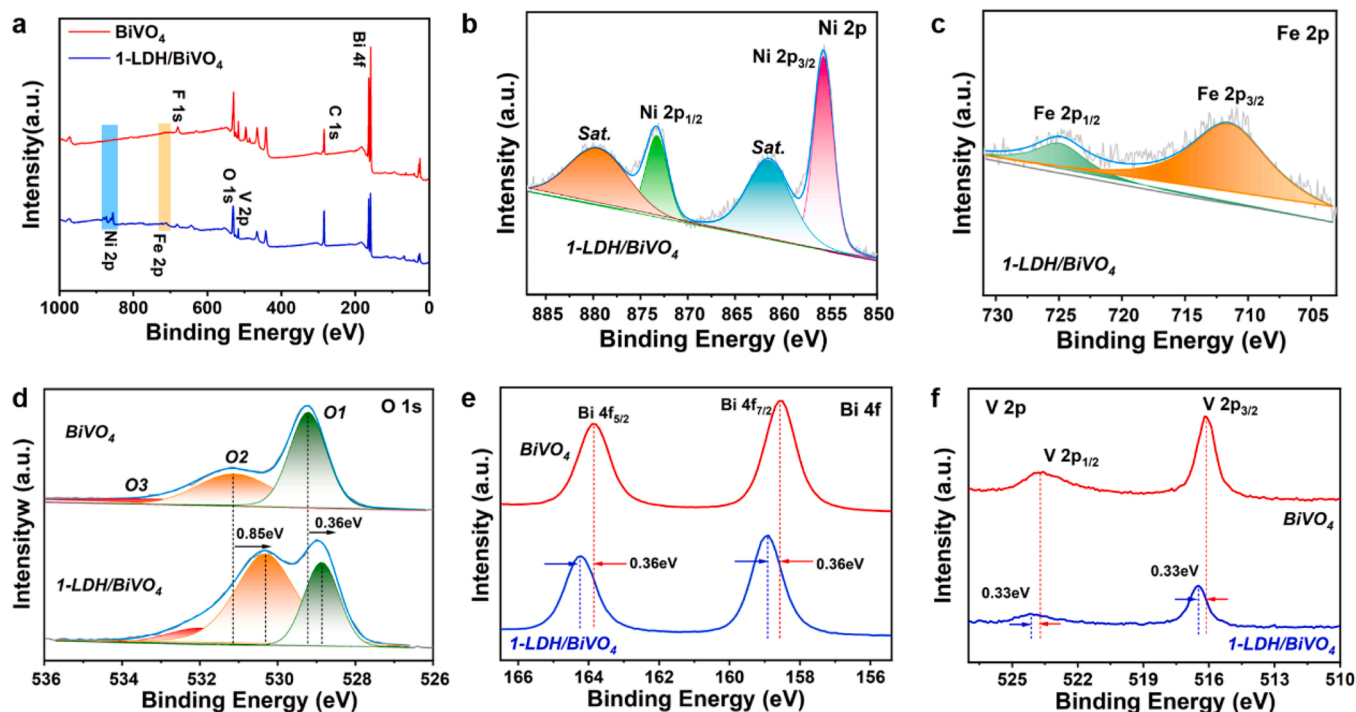

Fig. 3. XPS spectra. (a) Survey scan, (b) Ni 2p, (c) Fe 2p, (d) O 1 s, (e) Bi 4 f and (f) V 2p spectra of BiVO$_4$ and 1-LDH/BiVO$_4$.

while those at 516.1 and 523.7 eV are assigned to V^{5+} (Fig. 3f). Impressively, the negative shifts of O 1 s and positive shifts of Bi 4 f and V 2p in 1-LDH/BiVO$_4$ with respect to bare BiVO$_4$ suggest the strong electron transfer from BiVO$_4$ to NiFe-LDH.

3.2. Effect of TEMPO mediator

Water oxidation (i.e., OER) at the anode is considered to be the major competing reaction upon PEC oxidation of HMF in aqueous media. In this regard, the PEC oxidation of HMF, TEMPO mediator and water were first examined in H-cell. The LSV curve of BiVO$_4$ obtained without HMF and TEMPO exhibits an onset potential of ca. 0.30 V_{RHE} and a photocurrent of ~1.57 mA cm^{-2} at 1.23 V_{RHE} for water oxidation evolved into O$_2$ (Fig. 4a). When adding TEMPO, strongly decreased photocurrent is observed at potential below 0.95 V_{RHE} owing to the strong adsorption of TEMPO on the surface of BiVO$_4$. While the photocurrent increases markedly when potential is larger than 0.95 V_{RHE}, contributed by TEMPO oxidation reaction. Upon addition of HMF into TEMPO containing electrolyte, the photocurrent greatly increases owing effective TEMPO mediated HMF oxidation[23], accompanied by the suppression of water oxidation. The concentration of TEMPO has been varied to

further explore the role of redox mediator (Fig. S6a). The photocurrent increases at higher potential (>1.0 V_{RHE}) upon increasing TEMPO concentration from 1 to 3 mg mL^{-1}. The PEC oxidation of HMF at a constant potential of 1.0 V_{RHE} for 7 h was executed at varied TEMPO concentration. It can be found that HMF can be completely converted to FDCA with ~100 % selectivity when changing TEMPO concentration from 1 to 3 mg mL^{-1} (Fig. 4b). Impressively, the FE (93.9 %) in 3 mg mL^{-1} TEMPO is ~1.5 times that of 1 mg mL^{-1} TEMPO (74.7 %). The comparative results manifest a higher TEMPO concentration would promote the PEC oxidation of HMF with a desirable FE and facilitated reaction kinetics.

Similar results can be found in 1-LDH/BiVO$_4$. Noteworthy, TEMPO mediated HMF oxidation reaction is favored at a much lower potential (e.g. 0.7 V_{RHE}, Fig. 4c). The PEC oxidation of HMF at a constant potential of 0.7 V_{RHE} for 6 h was executed with 3 mg mL^{-1} of TEMPO. The complete consumption of HMF requires ~55 C charge passed to upgrade to FDCA (Fig. 4d) and the detected intermediates indicate the reaction pathway as follows: HMF→DFF→FFCA→FDCA (Fig. S7). While the results are absolutely different in the absence of TEMPO (Fig. 4e). The HMF conversion is 47.5 % and no FDCA can be found. The main oxidation products are DFF (yield of 20.0 %) and FFCA (yield of 27.4 %),
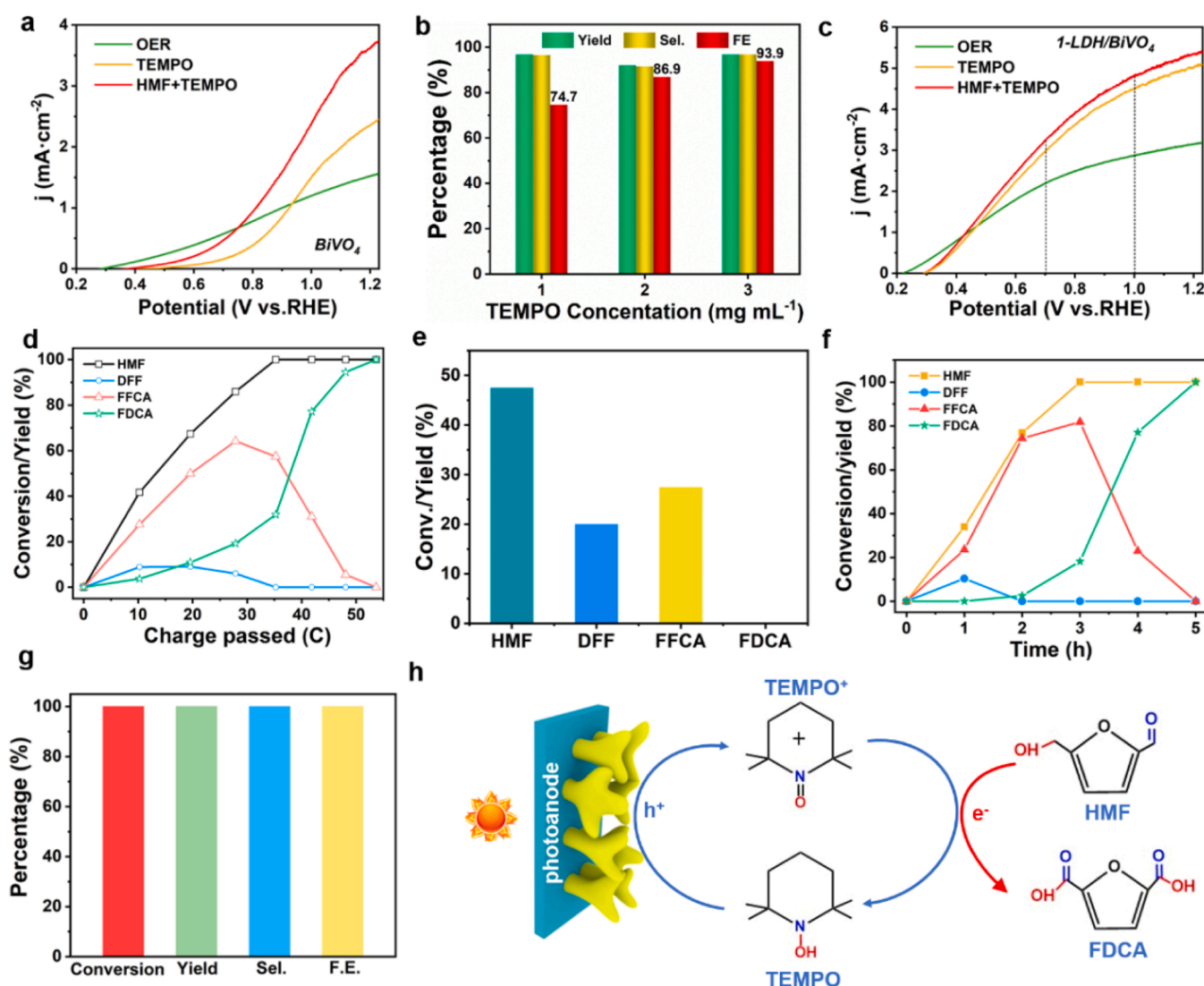

Fig. 4. LSV curves with/o TEMPO in borate buffer over (a) BiVO$_4$ and (c) 1-LDH/BiVO$_4$. (b) PEC oxidation results over BiVO$_4$ photoanode at varied TEMPO concentration. (d) The concentration changes of organic products during electrolysis at 0.7 V_{RHE} with 3 mg mL^{-1} TEMPO over 1-LDH/BiVO$_4$ photoanode. (e) The product distribution at 0.7 V_{RHE} without TEMPO. (f) The concentration changes of organics and (g) final electrolytic results at 0.6 V_{RHE} with 5 mg mL^{-1} TEMPO over 1-LDH/BiVO$_4$ photoanode. (h) Scheme of the TEMPO-mediated PEC oxidation of HMF.

implying that TEMPO mediator has high selectivity for the final oxidation product FDCA, and promotes the reaction kinetics. When increasing the TEMPO concentration to 5 mg mL^{-1}, the onset potential is apparently negatively shifted along with distinct photocurrent enhancement, especially below 0. 7 V$_{RHE}$ (Fig. S6b). A much smaller potential (0.6 V$_{RHE}$) is adopted to continuous PEC oxidation of HMF with 5 mg mL^{-1} of TEMPO. It is found that HMF can be completely converted to FDCA (yield of ~100 %) in 5 h with a FE of 100 % (Fig. 4f,g). In addition, the concentration of HMF is further increased from 5 mM to 10 mM and it takes 10 h to completely convert HMF to FDCA with ~100 % selectivity and ~100 % FE at 1.0 V$_{RHE}$ (Fig. S8). Based on the above results, the TEMPO-mediated HMF oxidation driven by solar energy has been proposed. The cyclic voltammetry (CV) curves reveal the typical redox behavior of TEMPO under dark [22,45]. It can be oxidized to TEMPO$^+$ by anodic current and subsequently reduced back on the cathodic sweep (Fig. S9). Upon light illumination, the generated holes from valence band of BiVO$_4$ can readily oxidize TEMPO to TEMPO$^+$, which then react with HMF and recover back to TEMPO. The applied potential is to enhance the separation of electron-hole pairs and make more holes available at the electrode surface for oxidation reaction [21]. As a result, the anodic current remarkably increases due to the regeneration of TEMPO (Fig. 4 h), and the cathodic current disappears as

TEMPO$^+$ is consumed by HMF oxidation [46]. The total content of TEMPO is maintained after continuous PEC oxidation as indicated from the integral area under CV curves (Fig. S10).

3.3. Effect of NiFe-LDH co-catalyst

The PEC performance of LDH/BiVO$_4$ photoanodes with different loading of NiFe-LDH cocatalyst was further investigated and the concentration of TEMPO mediator was fixed at 3 mg mL^{-1}. The OER performance (Fig. S11) indicates that 1-LDH/BiVO$_4$ with an optimal loading amount endows the largest photocurrent (3.18 mA cm^{-2}) at 1.23 V$_{RHE}$, which is twice that of pristine BiVO$_4$. Similarly, the photocurrent of the four LDH/BiVO$_4$ photoanodes for TEMPO-mediated PEC oxidation follows the same trend: 1-LDH/BiVO$_4$ > 0.5-LDH/BiVO$_4$ > 2-LDH/BiVO$_4$ > 4-LDH/BiVO$_4$ (Fig. 5a). Therefore, 1-LDH/BiVO$_4$ is chose as the optimal composite photoelectrode. Specifically, 1-LDH/BiVO$_4$ photoanode endows a superior photocurrent density of 3.54 mA cm^{-2} at 0.7 V$_{RHE}$, which is 7 times as high as that of pristine BiVO$_4$ (0.48 mA cm^{-2}, Fig. 5b). The onset potential of 1-LDH/BiVO$_4$ is dramatically reduced from 0.68 V$_{RHE}$ to 0.31 V$_{RHE}$ with a cathodic shift of 370 mV [25,47], which suggests that PEC oxidation of HMF is thermodynamically and kinetically favorable over LDH/BiVO$_4$ electrode.
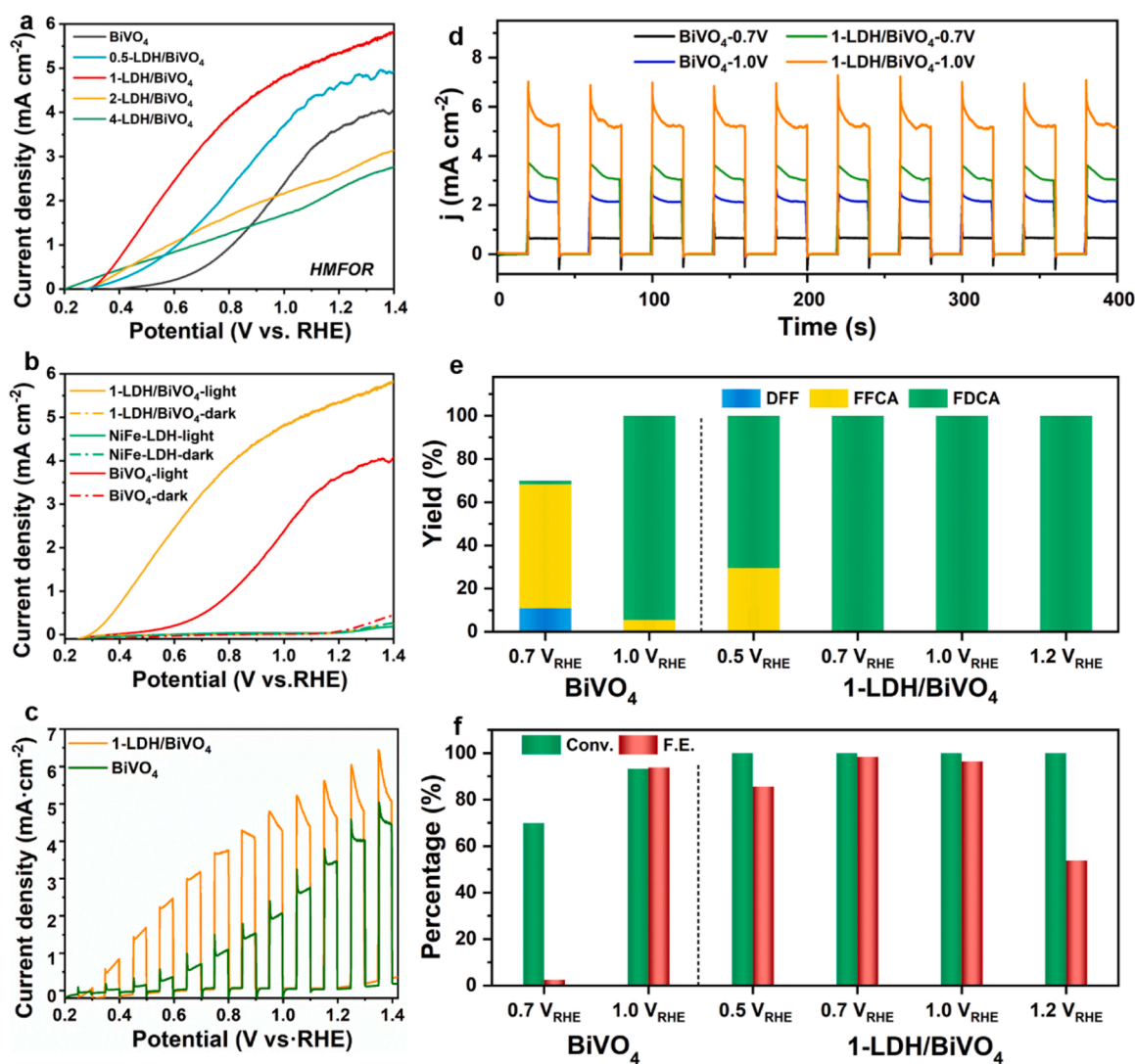
Fig. 5. (a) LSV curves of different photoanodes for PEC oxidation of HMF, (b) LSV curves under light illumination and under dark (dashed lines). (c) Chopped LSV curves. (d) I-t curves at 0.7 V$_{RHE}$ and 1.0 V$_{RHE}$ over 1-LDH/BiVO$_4$ and BiVO$_4$ photoanodes. (e) Yield of organic products and (f) conv. of HMF and FE over BiVO$_4$ and 1-LDH/BiVO$_4$ at different potentials.

Impressively, NiFe-LDH electrode has negligible photocurrent response in the potential region of 0.2–1.2 V. As an excellent electrocatalyst for HMF electrochemical oxidation, NiFe-LDH requires a relatively higher potential (>1.3 V) to oxidize HMF in 1 M KOH electrolyte [48]. Thus it cannot afford enough overpotential to drive this reaction in the buffer electrolyte herein. Transient photocurrent response under chopped light illumination (Fig. 5c) demonstrates rapid and repeatable response, in line with the LSV curves in Fig. 5b. The steady and reproducible photocurrent response at 0.7 and 1.0 V_{RHE} indicates the robust stability of the two photoanodes (Fig. 5d). The readily observed significant current spikes of 1-LDH/BiVO₄ upon light switching suggest the highly improved charge separation behavior and hole accumulation effect [41, 49].

Different potentials (0.5, 0.7, 1.0 and 1.2 V_{RHE}) were chosen to photoelectrolytic HMF to FDCA and the results are presented in Fig. 5e,f and Table S1. The final yield of FDCA over pristine BiVO₄ photoanode increases from 1.7 % at 0.7 V_{RHE} to 94.5 % at 1.0 V_{RHE}, indicating that the product yield is potential dependent. Accordingly, the FE. increases from 2.5 % (HMF conversion of 70.0 %) at 0.7 V_{RHE} to 93.9 % at 1.0 V_{RHE} (HMF conversion of 93.3 %). In contrast, the final yield of FDCA over 1-LDH/BiVO₄ can reach ~100 % at both two potentials accompanied by almost 100 % HMF conversion and 100 % FE. The electrolytic results undoubtedly confirm the positive effect of LDH loading on PEC oxidation of HMF to FDCA. Specifically, if we reduce the potential to 0.5 V_{RHE}, HMF cannot completely convert to FDCA (yield of 70.5 %) and the FE. is 85.6 %, indicating that more time is needed to further oxidize FFCA to FDCA. While if we raise the potential to 1.2 V_{RHE}, the conversion can be completed with FDCA yield of ~100% but a low FE of 53.8 %, suggesting that water oxidation takes place at this high potential. The results verify that the optimal potential is found to be 0.7 V_{RHE} for the composite electrode. Moreover, no oxidation product can be found when electrolysis at 0.7 V_{RHE} under dark over 1-LDH/BiVO₄ (Fig. S12), manifesting that the electrolytic potential can be effectively reduced under the assistance of solar energy. The XPS spectra (post in Fig. S13), SEM (Fig. S14) and TEM results (Fig. S15) of 1-LDH/BiVO₄ after continuous PEC oxidation of HMF reveal very little change compared with those tested on fresh sample, validating the excellent stability of composite photoanode.

The photocurrent relaxation kinetics are examined using transient photocurrent spectroscopy at potentiostatic conditions (0.7 V_{RHE} and 1.0 V_{RHE}, Fig. S16) and the transient decay time τ is represented by the logarithmic plots of D (Eq. 5) as a function of time, in which I_t is the
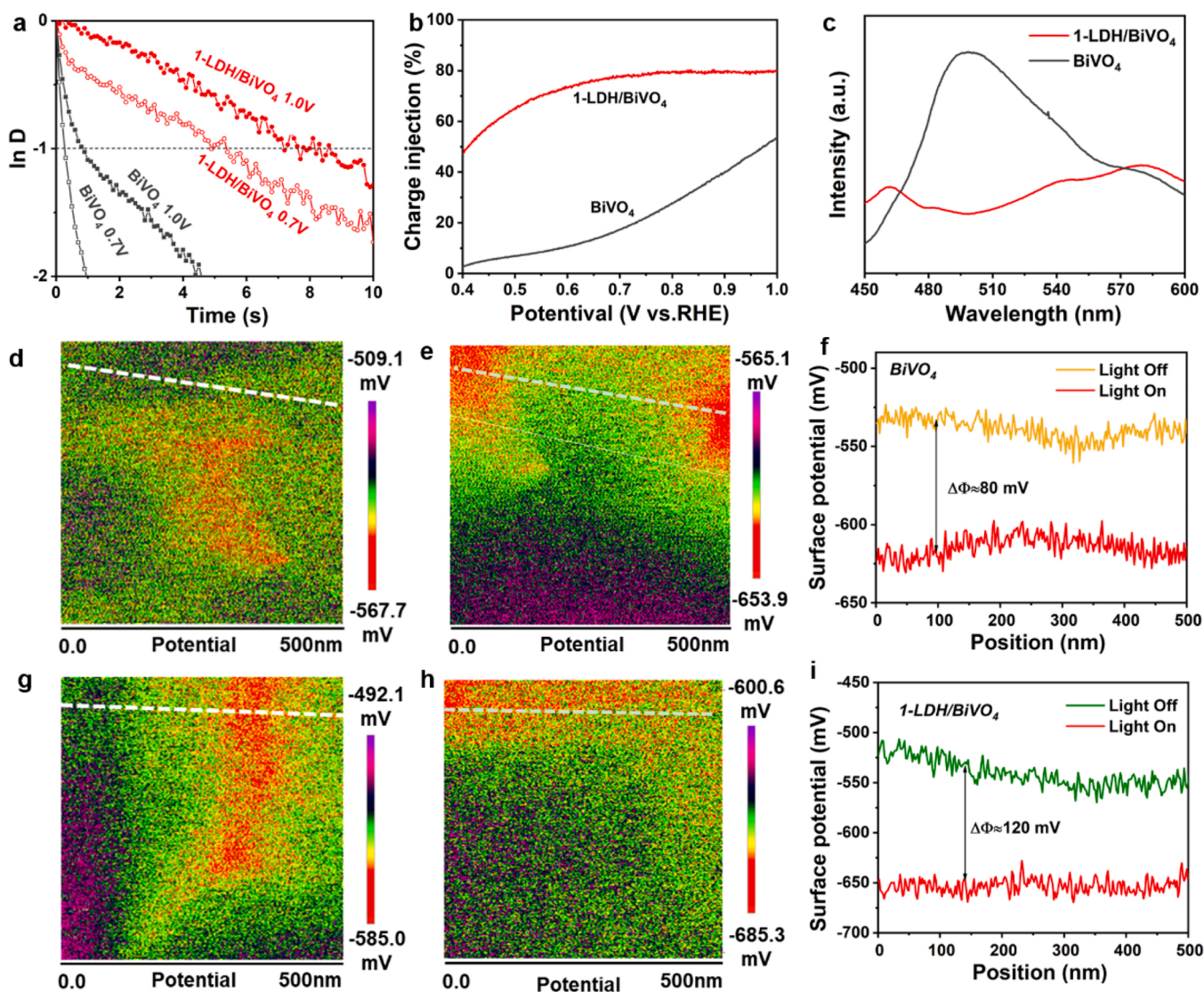
Fig. 6. (a) Plots of ln D versus time of BiVO₄ and 1-LDH/BiVO₄ for PEC oxidation of HMF at 0.7 V_{RHE} and 1.0 V_{RHE}. (b) Charge separation efficiency versus applied potential. (c) PL spectra. KPFM results. Surface potential images (d,g) under dark and (e,h) under light of BiVO₄ and 1-LDH/BiVO₄, respectively. (f,i) Surface potential difference (SPD, ΔΦ) curves along lines of BiVO₄ and 1-LDH/BiVO₄, respectively.

photocurrent at time t, I_{int} and I_{ph} are referred to the photocurrent at initial state and steady state, respectively. [30,50].

$$D = \frac{I_t - I_{ph}}{I_{int} - I_{ph}} \quad (5)$$

The nonlinear relationship implies the complex decay mechanism and the value of τ is always taken where $\ln D = -1$, which reflects the electronic lifetime of the semiconductor bulk (Fig. 6a). Pristine BiVO$_4$ photoanode suffers from fast charge recombination due to the sluggish charge-transfer kinetic at the semiconductor-electrolyte interface.[27] Impressively, the decay time τ of 1-LDH@BiVO$_4$ largely increases to 5.4 s at 0.7 V$_{RHE}$ and 7.9 s at 1.0 V$_{RHE}$, which is 18 times and 9.8 times as high as those of BiVO$_4$ (~0.3 s at 0.7 V$_{RHE}$ and 0.8 s at 1.0 V$_{RHE}$), respectively. It can be ascribed to the unreacted holes on the catalyst surface transferring to the reagent in electrolyte, resulting in prolonged carrier lifetime. The photo-generated charge injection efficiency (η_{inj}) was examined based on Eq. (6) using a typical hole scavenger of Na$_2$SO$_3$, where J_{HMF} and $J_{Na_2SO_3}$ are the photocurrent density for PEC oxidation of HMF and Na$_2$SO$_3$ oxidation, respectively, and the hole injection efficiency is assumed to be 100 %[41].

$$\eta_{inj}(\%) = J_{HMF}/J_{Na_2SO_3} \quad (6)$$

The η_{inj} of 1-LDH/BiVO$_4$ is 50 % greater than that of pristine BiVO$_4$ in the entire potential range calculated (Fig. 6b), indicating the significantly enhanced hole transfer capability and effectively suppressed charge recombination[28]. It reaches 77.6 % at 0.7 V$_{RHE}$ while that of BiVO$_4$ is 17.5 %. The incident photon-to-electron conversion efficiency (IPCE) was conducted to determine the quantitative correlation of light absorption at different wavelengths. A tremendous photocurrent enhancement can be achieved on 1-LDH/BiVO$_4$ with a maximal IPCE of 77.5 % at 460 nm (Fig. S17), twice higher than that of BiVO$_4$ (35.0 %).

Furthermore, the recombination of photoinduced electron-hole pairs can be reflected by Photoluminescence (PL) spectra (Fig. 6c). The strongly suppressed PL intensity of 1-LDH/BiVO$_4$ in the region of 450–600 nm suggests that the fluorescence-associated recombination of electron-hole pairs is significantly restrained, meaning higher separation efficiency of carriers than pristine BiVO$_4$. KPFM was further performed to reveal the spatial charge distribution in order to corroborate the charge separation/transfer process[51,52]. The atomic force microscope (AFM) height mapping images (Fig. S18) demonstrate that parental nanoporous BiVO$_4$ crystals turn out to be mesoporous with many tiny particles for 1-LDH/BiVO$_4$. Furthermore, the surface potential of the two electrodes was tested by KPFM under dark (Fig. 6d,g) and under light illumination (Fig. 6e,h). The more negative surface potential upon light illumination can be due to the photoexcited charge diffusing to the opposite direction of the catalyst driven by the potential difference, thus reducing the surface potential of charge screening effect[53]. The surface potential difference (SPD, $\Delta\Phi$) between under illumination and under dark can be defined as follows:

$$\Delta\Phi = surface\ potential_{(dark)} - surface\ potential_{(light)} \quad (7)$$

The surface potential under light of 1-LDH/BiVO$_4$ significantly increases and the resultant distinctly larger SPD ($\Delta\Phi$, Fig. 6f,i) is measured to be ca. 120 mV, 1.5 times that of BiVO$_4$, which definitely suggests that the composite photoanode endows much stronger electric field beneficial for the fast separation and transfer of photogenerated charges. Moreover, the charge transfer property at the photoanode/electrolyte interface was examined by the electrochemical impedance spectra (EIS, Fig. S19). As reported [41], the second arc at the low frequency region represents the charge transfer resistances (R$_{ct}$) at the electrode/electrolyte interface. The much smaller value fitted by the equivalent circuit (inset) of 1-LDH/BiVO$_4$ (20.01 Ω) than that of pristine BiVO$_4$ (702.20 Ω) validates a fast faradaic process and a favorable charge-transfer kinetics.

3.4. Proposed working mechanism

First-principle DFT calculations were performed to gain considerable insight into the organic adsorption behavior on the surface of photoanodes. The charge density difference contour and Bader charge analysis (Fig. 7a,b) clearly demonstrate that a greater charge transfer occurs between TEMPO molecule and BiVO$_4$ (~0.42 electrons) while only ~0.17 electrons are transferred from HMF to BiVO$_4$, which definitely verifies the strong capturing ability towards TEMPO. Similar phenomenon has been found in the case of LDH/BiVO$_4$ heterostructure (Fig. 7c, d). Moreover, obvious charge redistributions and significant electron transfer from TEMPO (0.49 electrons)/HMF (0.26 electrons) to LDH/BiVO$_4$ can be found, which supports the strong interactions between the organic substrates and the heterostructure photoanode. Specifically, the adsorption energy of HMF/TEMPO on the surface of BiVO$_4$ and LDH/BiVO$_4$ photoanodes can be calculated using the following equation:

$$\Delta E_{ads} = E_{total} - E_{surface} - E_{molecule} \quad (8)$$

in which E$_{total}$ represents the energy of HMF/TEMPO molecules adsorbed on the surface of BiVO$_4$ and LDH/BiVO$_4$, E$_{surface}$ and E$_{molecule}$ represent the energy of catalyst and organic molecule, respectively. The more negative values of ΔE_{ads}, the more stable of the HMF/TEMPO molecules adsorbed on BiVO$_4$ and LDH/BiVO$_4$ surfaces. As revealed in Fig. 7e, TEMPO is more easily adsorbed on the surface of both BiVO$_4$ and LDH/BiVO$_4$ compared to HMF, which further elucidate the strong binding strength to TEMPO. The more negative values obtained on LDH/BiVO$_4$ also suggest favorable adsorption behavior. Density of states (DOS) of BiVO$_4$ (Fig. S20a) reveal a semiconductor characteristics, giving rise to a band gap of ~2.14 eV. While the LDH/BiVO$_4$ (Fig. S20b) exhibits the metallic feature due to the formation of heterostructure and the DOS contributions near the Fermi level mainly come from the Fe 3d orbitals. The construction of heterostructure enhances the electronic conductivity and facilitates fast redox reaction kinetics, thereby improving the binding strength towards HMF and TEMPO. Collectively, the calculation results reveal that the PEC oxidation of HMF is more favorable via the TEMPO mediated pathway and the oxidation ability can be effectively enhanced by the introduction of heterostructure interface, which is consistent with the experimental results.

The optical properties are further investigated in order to disclose the band alignment of LDH/BiVO$_4$ heterostructure. A typical absorbance onset at ~510 nm is observed in the UV-Vis diffuse reflectance spectrum (DRS) for pristine BiVO$_4$ with a calculated optical band gap of 2.51 eV (Fig. S21). After NiFe-LDH loading, the absorption edge of 1-LDH/BiVO$_4$ is apparently red-shifted to 605 nm, resulting in a wider visible light absorption region, which endows an increase in light harvesting. The decreased optical band gap of 1-LDH/BiVO$_4$ (2.23 eV) also indicates the enhanced solar light absorption capability which is beneficial for PEC activity. The positive slopes of Mott-Schottky (MS) plots for BiVO$_4$ and NiFe-LDH (Fig. S22) indicates the characteristics of n-type semiconductors. Since the conduction band (CB) position of n-type semiconductor is generally assumed to be ~0.1 eV negative than the flat band potential [54,55], the CB position could be estimated to be 0.55 and 0.37 eV for BiVO$_4$ and NiFe-LDH, respectively. As a result, the potential of valance band (E$_{VB}$) can be obtained using formula: E$_{VB}$-E$_{CB}$=E$_g$, which is calculated to be 3.16 and 2.66 eV, respectively. In this regard, a type II band alignment is formed between BiVO$_4$ and NiFe-LDH as illustrated in Fig. 7f. The photoexcited electron-hole pairs are generated in both BiVO$_4$ and NiFe-LDH upon light illumination. Afterwards, the photoexcited electrons are collected by the CB of BiVO$_4$, and the photoexcited holes migrate to the opposite direction of the VB of NiFe-LDH. Therefore, an efficient photo-excited charge separation is obtained at the interface of BiVO$_4$ and NiFe-LDH heterojunction, and more holes are available to oxidize TEMPO mediators to TEMPO$^+$. Compared with direct oxidation, TEMPO-mediated HMF photooxidation is kinetically and thermodynamically more favorable than TEMPO
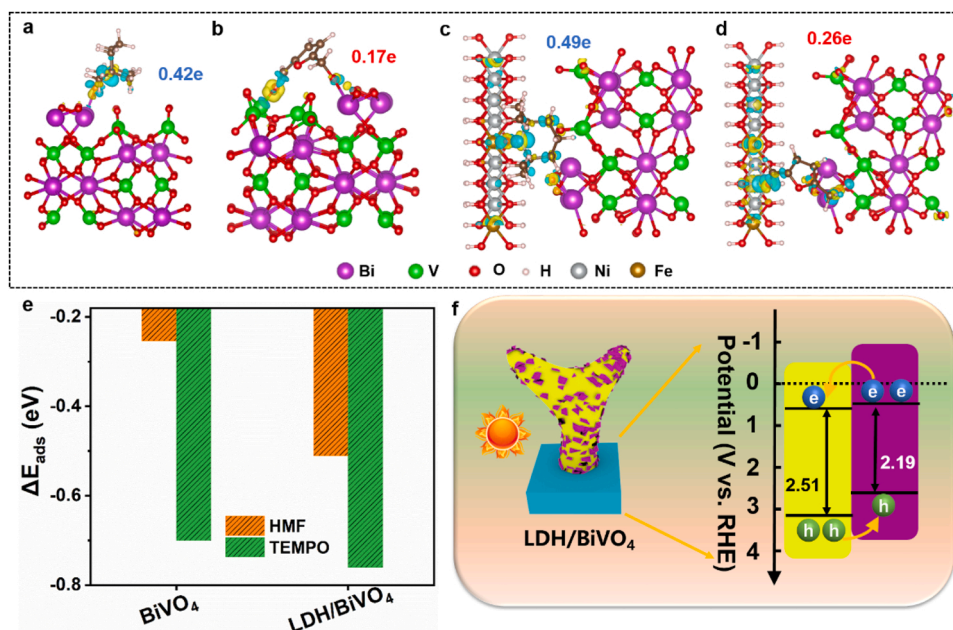
Fig. 7. The charge density difference diagrams of (a,c) TEMPO and (b,d) HMF anchored on $BiVO_4$ and $LDH/BiVO_4$ configurations, respectively. The iso-surface values are set to be $0.003e \text{ Å}^{-3}$. The charge accumulation and depletion are indicated by yellow and cyan area, respectively. (e) Calculated adsorption energy of HMF and TEMPO molecules on $BiVO_4$ and $LDH/BiVO_4$. (f) The band alignment of $LDH/BiVO_4$.

oxidation and water oxidation, demonstrating superior reaction selectivity and splendid Faradaic efficiency. Considering the wide versatility to alcohol-containing organics, TEMPO-catalyzed oxidation is readily applicable to a large variety of biologically derived organics [56,57], e. g., benzyl alcohol.

4. Conclusion

Heterostructure photoanodes consisted of nanoporous $BiVO_4$ films coating with NiFe-LDH cocatalysts are facilely developed for TEMPO mediated PEC oxidation of HMF. The effect of mediator concentration and cocatalyst loadings on the reaction kinetics and Faradaic efficiency are carefully investigated. The results disclose that superb reactivity with higher FE can be achieved with an increase of TEMPO concentration. Benefitted from the appropriate loading of NiFe-LDH cocatalyst, more efficient TEMPO-mediated HMF photooxidation is accomplished with a dramatically reduced electrolytic potential (from 1.0 V_{RHE} to 0.7 V_{RHE}) and highly boosted FE (from 2.5 % to $\sim$100 % at 0.7 V_{RHE}), demonstrating better energy utilization efficiency. The effective separation of photogenerated carriers of $LDH/BiVO_4$ photoanode indicates that more holes are available to oxidize TEMPO, leading to facilitated reaction kinetics. DFT calculations further confirm the optimized adsorption behaviors towards TEMPO and HMF, and the effectively enhanced oxidation ability on heterostructure photoanode.

CRediT authorship contribution statement

Lingxia Zheng: Conceptualization, Supervision, and Writing – review & editing. **Penghui Xu:** Manuscript preparation, Experimental Measurements. **Yujuan Zhao:** Data analysis. **Zhenyu Bao:** Data curation. **Xingyu Luo:** Theoretical simulation. **Xiaowei Shi:** Writing–review & editing. **Qi Wu:** Software, Review & editing. **Huajun Zheng:** Supervision, and Funding acquisition.

Declaration of Competing Interest

The authors declare that they have no known competing financial interests or personal relationships that could have appeared to influence the work reported in this paper.

Data availability

Data will be made available on request.

Appendix A. Supporting information

Supplementary data associated with this article can be found in the online version at doi:10.1016/j.apcatb.2023.122679.

References

[1] L. Wang, R. Wang, T. Qiu, L. Yang, Q. Han, Q. Shen, X. Zhou, Y. Zhou, Z. Zou, Bismuth vacancy-induced efficient CO_2 photoreduction in BiOCl directly from natural air: a progressive step toward photosynthesis in nature, Nano Lett. 21 (2021) 10260–10266.

[2] X. Wang, J. He, J. Li, G. Lua, F. Dong, T. Majima, M. Zhu, Immobilizing perovskite $CsPbBr_3$ nanocrystals on Black phosphorus nanosheets for boosting charge separation and photocatalytic CO_2 reduction, Appl. Catal. B Environ. 277 (2020), 119230.

[3] B. You, X. Liu, N. Jiang, Y. Sun, A general strategy for decoupled hydrogen production from water splitting by integrating oxidative biomass valorization, J. Am. Chem. Soc. 138 (2016) 13639–13646.

[4] H. Zhao, D. Lu, J. Wang, W. Tu, D. Wu, S.W. Koh, P. Gao, Z.J. Xu, S. Deng, Y. Zhou, B. You, H. Li, Raw biomass electroreforming coupled to green hydrogen generation, Nat. Commun. 12 (2021) 2008.

[5] G. Zhang, X. Yuan, B. Xie, Y. Meng, Z. Ni, S. Xia, S vacancies act as a bridge to promote electron injection from Z-scheme heterojunction to nitrogen molecule for photocatalytic ammonia synthesis, Chem. Eng. J. 433 (2022), 133670.

[6] Y. He, C. Zhang, J. Hu, M.K.H. Leung, NiFe-layered double hydroxide decorated $BiVO_4$ photoanode based bi-functional solar-light driven dual-photoelectrode photocatalytic fuel cell, Appl. Energy 255 (2019), 113770.

[7] G. Yin, C. Liu, T. Shi, D. Ji, Y. Yao, Z. Chen, Porous $BiVO_4$ coupled with $CuFeO_2$ and NiFe layered double hydroxide as highly-efficient photoanode toward boosted photoelectrochemical water oxidation, J. Photochem. Photobiol. A Chem. 426 (2022), 113742.

[8] D. He, R.-T. Gao, S. Liu, M. Sun, X. Liu, K. Hu, Y. Su, L. Wang, Yttrium-induced regulation of electron density in NiFe layered double hydroxides yields stable solar water splitting, ACS Catal. 10 (2020) 10570–10576.

[9] Y.X. Chen, A. Lavacchi, H.A. Miller, M. Bevilacqua, J. Filippi, M. Innocenti, A. Marchionni, W. Oberhauser, L. Wang, F. Vizza, Nanotechnology makes biomass electrolysis more energy efficient than water electrolysis, Nat. Commun. 5 (2014) 4036.

[10] B. Zhang, S. Yu, Y. Dai, X. Huang, L. Chou, G. Lu, G. Dong, Y. Bi, Nitrogen-incorporation activates NiFeOx catalysts for efficiently boosting oxygen evolution activity and stability of BiVO4 photoanodes, Nat. Commun. 12 (2021) 6969.

[11] Z. Zhao, H. Zhou, L. Zheng, P. Niu, G. Yang, W. Hu, J. Ran, S. Qiao, J. Wang, H. Zheng, Molecules interface engineering derived external electric field for effective charge separation in photoelectrocatalysis, Nano Energy 42 (2017) 90–97.

[12] L. Zheng, F. Teng, X. Ye, H. Zheng, X. Fang, Photo/electrochemical applications of metal sulfide/TiO2 heterostructures, Adv. Energy Mater. 10 (2020), 1902355.

[13] L. Zheng, Z. Lv, P. Xu, H. Xu, M. Zhu, Y. Zhao, X. Shi, H.-E. Wang, H. Zheng, Defect engineering of Ni3S2 nanosheets with highly active (110) facets toward efficient electrochemical biomass valorization, J. Mater. Chem. A 10 (2022) 23244–23253.

[14] X. Pang, H. Bai, Y. Huang, H. Zhao, G. Zheng, W. Fan, Mechanistic insights for dual-species evolution toward 5-hydroxymethylfurfural oxidation, J. Catal. 417 (2023) 22–34.

[15] X. Pang, H. Bai, H. Zhao, W. Fan, W. Shi, Efficient electrocatalytic oxidation of 5-hydroxymethylfurfural coupled with 4-nitrophenol hydrogenation in a water system, ACS Catal. 12 (2022) 1545–1557.

[16] H. Zhao, X. Pang, Y. Huang, Y. Bai, J. Ding, H. Bai, W. Fan, Electrocatalytic reduction of 4-nitrophenol over Ni-MOF/NF: understanding the self-enrichment effect of H-bonds, Chem. Commun. 58 (2022) 4897–4900.

[17] H. Zhao, X. Pang, Y. Huang, Y. Bai, J. Ding, H. Bai, W. Fan, Ag/Ni-MOF heterostructure with synergistic enrichment and activation properties for electrocatalytic reduction of 4-nitrophenol, Chem. Commun. 58 (2022) 13499–13502.

[18] S. Albonetti, A. Lolli, V. Morandi, A. Migliori, C. Lucarelli, F. Cavani, Conversion of 5-hydroxymethylfurfural to 2,5-urandicarboxylic acid over Au-based catalysts: optimization of active phase and metal–support interaction, Appl. Catal. B Environ. 163 (2015) 520–530.

[19] S.D. Tilley, Recent advances and emerging trends in photo-electrochemical solar energy conversion, Adv. Energy Mater. 9 (2019) 1802877.

[20] L. Zheng, Y. Zhao, P. Xu, Z. Lv, X. Shi, H. Zheng, Biomass upgrading coupled with H2 production via a nonprecious and versatile Cu-doped nickel nanotube electrocatalyst, J. Mater. Chem. A 10 (2022) 10181–10191.

[21] H.G. Cha, K.S. Choi, Combined biomass valorization and hydrogen production in a photoelectrochemical cell, Nat. Chem. 7 (2015) 328–333.

[22] D.J. Chadderdon, L.P. Wu, Z.A. McGraw, M. Panthani, W. Li, Heterostructured bismuth vanadate/cobalt phosphate photoelectrodes promote TEMPO-mediated oxidation of 5–hydroxymethylfurfural, ChemElectroChem 6 (2019) 3387–3392.

[23] A. Kawde, M. Sayed, Q. Shi, J. Uhlig, T. Pullerits, R. Hatti-Kaul, Photoelectrochemical oxidation in ambient conditions using earth-abundant hematite anode: a green route for the synthesis of biobased polymer building blocks, Catalysts 11 (2021).

[24] K.-H. Ye, H. Li, D. Huang, S. Xiao, W. Qiu, M. Li, Y. Hu, W. Mai, H. Ji, S. Yang, Enhancing photoelectrochemical water splitting by combining work function tuning and heterojunction engineering, Nat. Commun. 10 (2019) 3687.

[25] S. Zhou, K. Chen, J. Huang, L. Wang, M. Zhang, B. Bai, H. Liu, Q. Wang, Preparation of heterometallic CoNi-MOFs-modified BiVO4: a steady photoanode for improved performance in photoelectrochemical water splitting, Appl. Catal. B Environ. 266 (2020), 118513.

[26] Y. Qi, J. Zhang, Y. Kong, Y. Zhao, S. Chen, D. Li, W. Liu, Y. Chen, T. Xie, J. Cui, C. Li, K. Domen, F. Zhang, Unraveling of cocatalysts photodeposited selectively on facets of BiVO4 to boost solar water splitting, Nat. Commun. 13 (2022) 484.

[27] C. Zachäus, F.F. Abdi, L.M. Peter, R. van de Krol, Photocurrent of BiVO4 is limited by surface recombination, not surface catalysis, Chem. Sci. 8 (2017) 3712–3719.

[28] X. Chang, T. Wang, P. Zhang, J. Zhang, A. Li, J. Gong, Enhanced surface reaction kinetics and charge separation of p-n heterojunction Co3O4/BiVO4 photoanodes, J. Am. Chem. Soc. 137 (2015) 8356–8359.

[29] M. Sun, C. Yuan, R.-T. Gao, R. Zhang, X. Liu, T. Nakajima, X. Zhang, Y. Su, L. Wang, A bridging coordination of urea tailoring metal hydroxides oxygen evolution catalysts promotes stable solar water splitting, Chem. Eng. J. 426 (2021) 131062.

[30] Y.-H. Wu, D.A. Kuznetsov, N.C. Pflug, A. Fedorov, C.R. Müller, Solar-driven valorisation of glycerol on BiVO4 photoanodes: effect of co-catalyst and reaction media on reaction selectivity, J. Mater. Chem. A 9 (2021) 6252–6260.

[31] X. Wang, H. Jiang, M. Zhu, X. Shi, Cascaded electron transition proved by femto-second transient absorption spectroscopy for enhanced photocatalysis hydrogen generation, Chin. Chem. Lett. 34 (2023), 107683.

[32] T. Li, T. Kasahara, J. He, K.E. Dettelbach, G.M. Sammis, C.P. Berlinguette, Photoelectrochemical oxidation of organic substrates in organic media, Nat. Commun. 8 (2017) 390.

[33] S.-j Xia, X.-b Zhou, W. Shi, G.-x Pan, Z.-m Ni, Photocatalytic property and mechanism studies on acid red 14 by MxOy/ZnTi–layered double hydroxides (M=Fe, Sn, Ce), J. Mol. Catal. A Chem. 392 (2014) 270–277.

[34] X. Liu, X. Wang, X. Yuan, W. Dong, F. Huang, Rational composition and structural design of in situ grown nickel-based electrocatalysts for efficient water electrolysis, J. Mater. Chem. A 4 (2016) 167–172.

[35] H. Sun, W. Zhang, J.-G. Li, Z. Li, X. Ao, K.-H. Xue, K.K. Ostrikov, J. Tang, C. Wang, Rh-engineered ultrathin NiFe-LDH nanosheets enable highly-efficient overall water splitting and urea electrolysis, Appl. Catal. B Environ. 284 (2021), 119740.

[36] G. Kresse, J. Furthmüller, Efficiency of ab-initio total energy calculations for metals and semiconductors using a plane-wave basis set, Comput. Mater. Sci. 6 (1996) 15–50.

[37] P.E. Blöchl, Projector augmented-wave method, Phys. Rev. B 50 (1994) 17953–17979.

[38] J.P. Perdew, K. Burke, M. Ernzerhof, Generalized gradient approximation made simple, Phys. Rev. Lett. 77 (1996) 3865–3868.

[39] G. Kresse, D. Joubert, From ultrasoft pseudopotentials to the projector augmented-wave method, Phys. Rev. B 59 (1999) 1758–1775.

[40] S. Stefan, A. Jens, E. Stephan, K. Helge, A consistent and accurate ab initio parametrization of density functional dispersion correction (DFT-D) for the 94 elements H-Pu, J. Chem. Phys. 132 (2010), 154004.

[41] J. Liu, J. Li, Y. Li, J. Guo, S.-M. Xu, R. Zhang, M. Shao, Photoelectrochemical water splitting coupled with degradation of organic pollutants enhanced by surface and interface engineering of BiVO4 photoanode, Appl. Catal. B Environ. 278 (2020), 119268.

[42] T.W. Kim, K.-S. Choi, Nanoporous BiVO4 photoanodes with dual-layer oxygen evolution catalysts for solar water splitting, Science 343 (2014) 990–994.

[43] J. Liu, J. Wang, B. Zhang, Y. Ruan, L. Lv, X. Ji, K. Xu, L. Miao, J. Jiang, Hierarchical NiCo2S4@NiFe LDH heterostructures supported on nickel foam for enhanced overall-water-splitting activity, ACS Appl. Mater. Interfaces 9 (2017) 15364–15372.

[44] P. Li, X. Duan, Y. Kuang, Y. Li, G. Zhang, W. Liu, X. Sun, Tuning electronic structure of NiFe layered double hydroxides with vanadium doping toward high efficient electrocatalytic water oxidation, Adv. Energy Mater. 8 (2018) 1703341.

[45] M.H. Furigay, S. Chaudhuri, S.M. Deresh, A.B. Weberg, P. Pandey, P.J. Carroll, G. C. Schatz, E.J. Schelter, Selective reduction of niobium(V) species to promote molecular niobium/tantalum separation, Inorg. Chem. 61 (2022) 23–27.

[46] X.H. Chadderdon, D.J. Chadderdon, T. Pfennig, B.H. Shanks, W. Li, Paired electrocatalytic hydrogenation and oxidation of 5-(hydroxymethyl)furfural for efficient production of biomass-derived monomers, Green Chem. 21 (2019) 6210–6219.

[47] T. Palaniselvam, L. Shi, G. Mettela, D.H. Anjum, R. Li, K.P. Katuri, P.E. Saikaly, P. Wang, Vastly enhanced BiVO4 photocatalytic OER performance by NiCoO2 as cocatalyst, Adv. Mater. Interfaces 4 (2017) 1700540.

[48] W.-J. Liu, L. Dang, Z. Xu, H.-Q. Yu, S. Jin, G.W. Huber, Electrochemical oxidation of 5-hydroxymethylfurfural with NiFe layered double hydroxide (LDH) nanosheet catalysts, ACS Catal. 8 (2018) 5533–5541.

[49] Y. Zhu, J. Ren, X. Yang, G. Chang, Y. Bu, G. Wei, W. Han, D. Yang, Interface engineering of 3D BiVO4/Fe-based layered double hydroxide core/shell nanostructures for boosting photoelectrochemical water oxidation, J. Mater. Chem. A 5 (2017) 9952–9959.

[50] A. Hagfeldt, H. Lindström, S. Södergren, S.-E. Lindquist, Photoelectrochemical studies of colloidal TiO2 films: the effect of oxygen studied by photocurrent transients, J. Electroanal. Chem. 381 (1995) 39–46.

[51] Z. Gu, X. An, R. Liu, L. Xiong, J. Tang, C. Hu, H. Liu, J. Qu, Interface-modulated nanojunction and microfluidic platform for photoelectrocatalytic chemicals upgrading, Appl. Catal. B Environ. 282 (2021) 119541.

[52] X.D. Wang, Y.H. Huang, J.F. Liao, Y. Jiang, L. Zhou, X.Y. Zhang, H.Y. Chen, D. B. Kuang, In situ construction of a Cs2SnI6 perovskite nanocrystal/SnS2 nanosheet heterojunction with boosted interfacial charge transfer, J. Am. Chem. Soc. 141 (2019) 13434–13441.

[53] X. Fan, Z. Wu, L. Wang, C. Wang, Exploring the Origin of High Dechlorination Activity in Polar Materials M2B5O9Cl (M = Ca, Sr, Ba, Pb) with Built-In Electric Field, Chem. Mater. 29 (2017) 639–647.

[54] S. Sun, W. Wang, D. Li, L. Zhang, D. Jiang, Solar Light Driven Pure Water Splitting on Quantum Sized BiVO4 without any Cocatalyst, ACS Catal. 4 (2014) 3498–3503.

[55] X. Shi, F. Dong, C. Dai, X. Ye, P. Yang, L. Zheng, H. Zheng, WO3/ZnIn2S4 heterojunction photoanodes grafting silane molecule for efficient photoelectrochemical water splitting, Electrochim. Acta 361 (2020), 137017.

[56] X. Chen, X. Zhong, B. Yuan, S. Li, Y. Gu, Q. Zhang, G. Zhuang, X. Li, S. Deng, J.-g. Wang, Defect engineering of nickel hydroxide nanosheets by Ostwald ripening for enhanced selective electrocatalytic alcohol oxidation, Green. Chem. 21 (2019) 578–588.

[57] B. Karimi, M. Ghahremani, R. Ciriminna, M. Pagliaro, New Stable Catalytic Electrodes Functionalized with TEMPO for the Waste-Free Oxidation of Alcohol, Org. Process Res. Dev. 22 (2018) 1298–1305.